Overview of gyrokinetic studies of finite- microturbulence

2015 Nucl. Fusion 55 104011

(http://iopscience.iop.org/0029-5515/55/10/104011)

IOP Publishing | International Atomic Energy Agency Nuclear Fusion
Nucl. Fusion **55** (2015) 104011 (12pp) doi:10.1088/0029-5515/55/10/104011

Overview of gyrokinetic studies of finite-β microturbulence

P.W. Terry[1], D. Carmody[1], H. Doerk[2], W. Guttenfelder[3], D.R. Hatch[4], C.C. Hegna[1], A. Ishizawa[5], F. Jenko[2,6], W.M. Nevins[7], I. Predebon[8], M.J. Pueschel[1], J.S. Sarff[1] and G.G. Whelan[1]

[1] University of Wisconsin-Madison, Madison, Wisconsin 53706, USA
[2] Max-Planck-Institut für Plasmaphysik, Boltzmannstr. 2, 85748 Garching, Germany
[3] Princeton Plasma Physics Laboratory, Princeton, New Jersey 08543, USA
[4] University of Texas at Austin, Austin, Texas 78712, USA
[5] National Institute for Fusion Science, 322-6 Oroshi-cho, Toki City, GIFU Prefecture 509-5292, Japan
[6] University of California, Los Angeles, Los Angeles, California 90095, USA
[7] Lawrence Livermore National Laboratory, Livermore, California 94551, USA
[8] Conzorzio RFX, Corso Stati Uniti 4, 35127 Padua PD, Italy

E-mail: pwterry@wisc.edu

Received 21 November 2014, revised 10 April 2015
Accepted for publication 23 April 2015
Published 19 June 2015

Abstract

Recent results on electromagnetic turbulence from gyrokinetic studies in different magnetic configurations are overviewed, detailing the physics of electromagnetic turbulence and transport, and the effect of equilibrium magnetic field scale lengths. Ion temperature gradient (ITG) turbulence is shown to produce magnetic stochasticity through nonlinear excitation of linearly stable tearing-parity modes. The excitation, which is catalyzed by the zonal flow, produces an electron heat flux proportional to β^2 that deviates markedly from quasilinear theory. Above a critical beta known as the non-zonal transition (NZT), the magnetic fluctuations disable zonal flows by allowing electron streaming that shorts zonal potential between flux surfaces. This leads to a regime of very high transport levels. Kinetic ballooning mode (KBM) saturation is described. For tokamaks saturation involves twisted structures arising from magnetic shear; for helical plasmas oppositely inclined convection cells interact by mutual shearing. Microtearing modes are unstable in the magnetic geometry of tokamaks and the reversed field pinch (RFP). In NSTX instability requires finite collisionality, large beta, and is favored by increasing magnetic shear and decreasing safety factor. In the RFP, a new branch of microtearing with finite growth rate at vanishing collisionality is shown from analytic theory to require the electron grad-B/curvature drift resonance. However, gyrokinetic modeling of experimental MST RFP discharges at finite beta reveals turbulence that is electrostatic, has large zonal flows, and a large Dimits shift. Analysis shows that the shorter equilibrium magnetic field scale lengths increase the critical gradients associated with the instability of trapped electron modes, ITG and microtearing, while increasing beta thresholds for KBM instability and the NZT.

Keywords: turbulence, electromagnetic, gyrokinetics

(Some figures may appear in colour only in the online journal)

1. Introduction

Numerical solutions of comprehensive gyrokinetic models for toroidal magnetic confinement configurations have provided an increasingly realistic picture of confinement-limiting instabilities and turbulence. In particular there is a significant and well-developed body of work devoted to understanding electrostatic turbulence and transport at zero β, where β is the ratio of plasma pressure to magnetic pressure. However, finite-β regimes are intrinsically of interest because they lead to increased fusion reaction rates, higher bootstrap current fraction, and potentially other desirable properties. Our understanding of turbulence and transport in magnetically confined plasmas at finite β from gyrokinetic simulation is less well developed than the zero-β case. The most well known piece of phenomenology is the way the dominant instabilities driving turbulence change character as β is increased, with the kinetic ballooning mode (KBM) ultimately supplanting the ion temperature gradient (ITG) and trapped electron mode (TEM) instabilities above a critical β [1–5]. Less is known about saturation, in part, because it can be difficult or computationally taxing to achieve realistic

and physically meaningful saturated states from numerical gyrokinetic models. However, what has been done, both with gyrokinetics and other models, suggests intriguing differences with zero-β cases, stemming from changes in instability growth rates, zonal flow drive, flow residuals, and fluctuation characteristics [6–9]. This paper offers an overview of recent gyrokinetic studies that probe and highlight new and modified physical effects operating at finite β. These effects relate to the origin of magnetic field stochasticity at very low β, the appearance of microtearing instabilities, the behavior of flows in the presence of stochasticity, the saturation of finite-β instabilities, and a consideration of the critical β-values for these effects, and their dependence on magnetic geometry.

The kinds of issues that arise in microturbulence at finite β are apparent from a consideration of past work. Most of the work has been done for tokamak plasmas. However, gyrokinetic modeling has shown that the same types of microinstabilities appear in tokamaks, stellarators and the reversed field pinch (RFP), with the dominant instability dependent on details of the configuration and equilibrium. It is well established that ion temperature gradient (ITG) instability becomes weaker as β increases [10–12] with complete stability in tokamaks typically at a critical β between 1% and 2% [13] and in RFPs between 6% and 10% [14]. In the tokamak, above the critical β for ITG stabilization, trapped electron mode (TEM) instability may continue, with a growth rate that is quite insensitive to β, while the kinetic ballooning mode (KBM) appears at a fraction of the ideal β limit, with a large growth rate that increases very strongly with β [11]. A characterization of the saturation of KBM has been lacking. Linearly unstable microtearing modes (MTM) [15–18] also arise above a critical β in simulations of discharges for standard tokamaks [19, 20], spherical tokamaks [21–24], and the reversed field pinch (RFP) [14, 25]. (For a review of microtearing modes see [26].) These observations have been somewhat surprising, given earlier theoretical indications of stability [27], but not altogether unanticipated [21]. In nonlinearly saturated ITG turbulence, zonal flow strength, as measured by its shearing rate, weakens as β increases, but not as strongly as the reduction of growth rate. The result is a saturation in which zonal flows play a larger role in a relative sense as β increases [13, 28, 29]. However, there is also a phenomenon observed in gyrokinetic simulation of ITG turbulence sometimes referred to as the high β runaway, where above a critical β transport fluxes diverge away from an apparently transient saturated level to very high values [30–32]. For the Cyclone base case the critical β for this phenomenon is a fraction (around 70%) of the KBM instability threshold. Even at very low β values of order 0.1%, magnetic fluctuations that lead to a stochastic field are observed in simulations of ITG turbulence [33]. The magnetic flutter transport from this field is small, but it rises quadratically as β increases. The source of the stochasticity, given the low β and predominant ballooning parity of ITG fluctuations has only been understood recently in work described below [34, 35]. It arises from a very general aspect of instability-driven plasma turbulence, namely, that nonlinearity excites a large array of damped modes in the scale range of the instability [36, 37]. It is important to understand the role of this phenomenon in turbulence saturation and transport at finite β.

Because the study of large-scale stable modes in saturation is still in its infancy, the physical details of saturation mechanisms are still not well understood. Historically, most saturation mechanisms have relied on damping at small scale, ignoring large-scale sinks from stable modes. Examples include the entropy cascade [38], the zonal flow paradigm [39], the secondary Kelvin–Helmholtz instability in the saturation of electron temperature gradient (ETG) instability [40], and reconnection [41, 42]. Processes like the entropy cascade describe energy transfer to small scale, where for steady state, the fluctuation energy must be damped. The entropy cascade provides a detailed picture of the forward cascade process in relation to the gyroaverage, but it is worth noting that the kinetic nonlinearity, as an advective derivative of the distribution, is fundamentally a forward cascade nonlinearity. The zonal flow paradigm invokes energy transfer to large scale zonal flows, but the primary saturation of the instability, given weak zonal flow damping, relies on zonal flow shearing, which enhances transfer to small scales. Where large-scale stable modes have been examined in relation to the above processes, their role has been significant in every case. The entropy cascade is subject to large scale damping from stable modes unless the collisionality is very weak [43] relative to present day fusion devices [44]. Large scale stable modes are the main energy sink in zonal-flow-regulated ITG turbulence, with zonal flows catalyzing transfer to the stable modes [45]. The secondary Kelvin–Helmholtz mode is a dissipative structure made up of damped roots of the primary ETG instability dispersion relation [46]. In each of these cases, the conventional saturation mechanisms mentioned at the beginning of this paragraph are operative, but the energy damping landscape is strongly modified by the stable modes. Consequently this type of physics needs to be considered in the context of saturation at finite β.

This overview focuses on physical processes that arise sequentially as β is increased from very low values, and whose underlying physics is interrelated. We begin with the phenomenon that emerges at the lowest β, where we show that the stochastic magnetic field in low β ITG turbulence arises from tearing parity stable modes that are excited to finite amplitude by the nonlinearity [34]. We next examine how magnetic fluctuations disable zonal flows, leading to the high β runaway. An effective island overlap criterion predicts the threshold, which is now more appropriately referred to as the non-zonal transition (NZT) to a new saturated state of very large fluxes [31]. The threshold criterion shows that NZT may occur at a critical β that is above or below that of the KBM instability, depending on the magnitude of the temperature gradient. In the former case, KBM grows and saturates in an environment where magnetic activity makes zonal flows weaker. We describe saturation of the KBM instability in both a standard tokamak equilibrium and for the 3D equilibrium of the Large Helical Device (LHD) [47]. Discharges in the National Spherical Torus Experiment (NSTX) and RFX-mod, a reversed field pinch (RFP), both operate at β values that are larger than those of standard tokamaks. Modeling of discharges in these devices show that the MTM is the dominant instability [23, 25]. We also show that the MTM is unstable in the Madison Symmetric Torus RFP [14], specifically looking at standard-confinement-type discharges where an important difference with the enhanced confinement discharges that occur with current profile control is the lower magnetic shear. In enhanced confinement discharges, recent modeling shows

turbulence that is surprisingly electrostatic in character. The fluctuations are density-gradient driven trapped electron modes (TEM) [48]. Despite a β of a few percent, modes like the MTM and KBM appear to be stable. The presence of a large Dimits shift and strong zonal flows indicates that the system is below the NZT threshold. The implication is that these thresholds are higher in the RFP than in the tokamak [48].

The fact that these discharges have a large magnetic shear, which is stabilizing for MTM, leads us to the last important element of this paper, an analysis of how magnetic configuration and its magnetic field scale lengths impact all of the processes described above. Noting that the same set of instabilities (ITG, KBM, MTM, TEM) can all arise in multiple magnetic configurations, comparisons across different configurations demonstrate the effect of magnetic configuration in the form of safety factor q, and magnetic field scale lengths. In configurations with smaller magnetic field scale lengths, the critical gradient thresholds for both the linear instability and the nonlinear fluxes are raised [48]. In such configurations the finite β thresholds both of stabilization (e.g. ITG) and destabilization (KBM) are also raised. Moreover, the critical β values for NZT and its large transport levels are raised. One type of device with these properties is the RFP. Simulations show that raising these thresholds through short magnetic field scale lengths yields critical gradients that are larger than those of tokamaks by a factor of 3. This suggests that short magnetic field scale lengths are quite favorable for maintaining steeper equilibrium profiles and greater stored energy in finite β discharges.

This overview is finite in scope and is not intended to cover every recent contribution from gyrokinetic simulation relating to microturbulence at finite β. For example, investigations involving impurities [49] or fast particle species [29, 50, 51] in finite β plasmas are not included. In particular, [29] and [51] illustrate that model agreement with experimental discharges requires accounting for the complex workings of multiple effects, in this case including the strengthening of zonal-flow saturation relative to instability at finite β, the stabilizing effect of fast particles, and mean sheared flows, among other things. The generally beneficial effects ascribed to β in [29] and [51] are consistent with past assays, which show that benefits of higher β are eventually undone by new magnetic phenomena like the KBM. In this overview our primary focus is on greater understanding of finite β effects without additional complicating factors.

2. Subdominant tearing parity modes

Many fundamental aspects of electromagnetic turbulence and transport have been discovered by studying a finite-β version of the Cyclone base case (CBC) parameters. Scans of β ranging from the electrostatic limit to the KBM limit demonstrate a significant decrease in electrostatic transport concurrent with an increasing electron electromagnetic heat flux that scales like β^2 and becomes comparable to the electrostatic channels as β nears the KBM limit. The electromagnetic transport has been shown to be produced by free-streaming electrons in the stochastic magnetic field produced by the turbulent magnetic fluctuations [13, 28, 33, 52, 53]. The onset of a chaotic magnetic field occurs at very low β, of order 0.1%, where the electron heat flux is still very small. An understanding of the electromagnetic transport relies on an understanding of the mechanisms that produce the turbulence-driven stochastic magnetic field. In the remainder of this section we describe those mechanisms, and the magnetic transport that results. We do not discuss here the electrostatic component, but it should be kept in mind that it dominates for low β and is only surpassed by the magnetic component near the KBM threshold.

The stochastic magnetic field of CBC ITG turbulence is an aspect of saturation. For unstable modes to saturate, they must couple through the nonlinearity to fluctuations that are damped, with amplitudes adjusting themselves to achieve a balance between energy input and dissipation. This process has long been viewed as occurring across the wavenumber spectrum. With instability residing in low wavenumbers perpendicular to the magnetic field in gyrokinetic turbulence and damping at high wave numbers due to collisions, the necessary coupling between the low and high wavenumbers could be provided by nonlinear energy transfer, as in the entropy cascade [38]. Under this type of scenario a perpendicular wavenumber cascade initiated by an electrostatic instability would be expected to involve purely electrostatic fluctuations at higher wavenumber. However, contrary to the standard picture, mode decompositions of the fluctuations in the CBC show that even at low wavenumbers where the instability resides, there are fluctuation components associated with parallel and velocity-space degrees of freedom that are distinct from the instability, quite unlike it, and in fact *are damped* [37, 54]. The net fluctuation can be decomposed into a mode basis, e.g. the eigenmodes of the linear gyrokinetic operator or a proper orthogonal decomposition. What these decompositions show is that at saturation a fluctuation in the perpendicular wavenumber range of the instability is comprised of the dominant unstable mode and many other modes. Most of these modes are stable. They make a large contribution to the removal of energy that balances the instability drive, and is not accounted for in descriptions of wavenumber cascades [45, 55] like the entropy cascade. Some of these modes are electromagnetic and create magnetic islands [34, 35]. It should be noted that stable modes are excited by the nonlinearity, and damp perpendicular wavenumber cascades irrespective of whether the cascades are forward or inverse.

Magnetic islands are produced by modes with tearing parity—a mode structure for the parallel magnetic vector potential $A_\parallel$ that is even for displacements along the magnetic field measured from the outboard midplane. ITG modes (centered at $k_x = 0$) are characterized by ballooning parity—odd-parity in $A_\parallel$—and thus would not be expected to produce significant magnetic stochasticity. There are two candidates for tearing-parity fluctuations in ITG-driven turbulence: (1) finite-k_x ITG modes, which are allowed to have a tearing-parity component, and (2) some other mode that is intrinsically characterized by tearing parity. There are multiple manifestations of modes in the latter category. Tearing parity ITG and ETG modes (TITG, TETG) are tearing-parity counterparts to the more familiar ITG and ETG modes, sharing their most salient properties with the exception of the parity of the mode structure. As such, they are

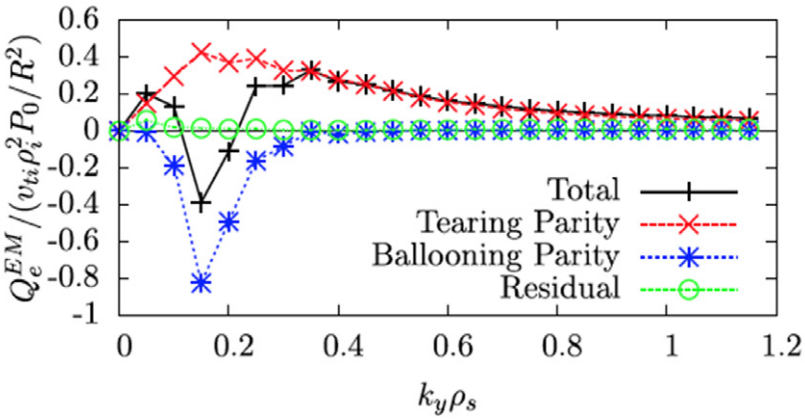

Figure 1. The total electromagnetic electron heat flux spectrum (plus signs), summed over k_x for $\beta = 0.003$, decomposed into contributions from tearing modes (crosses), ballooning modes (asterisks), and all remaining fluctuations (circles) (from [34]).

not intrinsically electromagnetic and have small components of the magnetic vector potential. Microtearing modes *are* intrinsically electromagnetic tearing parity modes (i.e. they cannot exist when $\beta = 0$), and are characterized by a large $A_\parallel$ component. Understanding electromagnetic transport relies on identifying which of these modes produces magnetic stochasticity and determining by which mechanism the modes are excited.

To identify the source of the stochasticity, proper orthogonal decompositions (POD) of the turbulence were constructed to isolate the important magnetic fluctuations [34]. PODs of $A_\parallel$ effectively capture the dominant tearing component and the dominant ballooning component in the first two POD modes. The POD is flexible enough to extract modes with slightly mixed-parity, which is characteristic of $k_x \neq 0$ ITG modes, and can thus distinguish between ITG-like modes with a small tearing component and other modes with a dominant tearing component. This procedure clearly identifies predominantly tearing-parity fluctuations as the mechanism for the magnetic stochasticity and transport, eliminating the ITG mode as the direct producer. A reconstruction of the electromagnetic flux using the POD decomposition demonstrates that the tearing-parity fluctuations produce outward heat flux, while the ballooning-parity fluctuations produce an inward flux (not stochastic) that is consistent with the quasilinear properties of the ITG mode. The distinctive spectrum that results from the superposition of these two mechanisms is shown in figure 1.

PODs of the actual gyrocenter distribution function were used to examine the detailed properties of the most important tearing-parity modes. A high-amplitude POD mode was identified that has properties similar to the corresponding linear microtearing mode (which is stable) and dissimilar from linear TITG and TETG modes (which are slightly unstable); the ratio of electromagnetic to electrostatic heat flux, and the ratio of the normalized $|A_\parallel|^2$ to the electrostatic potential $|\phi^2|$ for both the tearing parity POD mode and the linear MTM modes are orders of magnitude larger than the corresponding values for TITG and TETG modes. Moreover the $A_\parallel$ mode structures for the tearing-parity POD mode and the linear MTM mode are virtually identical. In short, the turbulence structures that produce the magnetic stochasticity correspond closely to stable MTMs that are identified in the linear eigenmode spectrum.

The POD modes were also used to project out the component of the nonlinear energy transfer that drives the microtearing fluctuations. It was shown that coupling to zonal $k_y = 0$ modes was the dominant nonlinear excitation mechanism. Further evidence of the nonlinear nature of the electromagnetic transport is found in the early-time dynamics of the flux components; the electrostatic fluxes increase in the early linear phase at a rate consistent with the dominant ITG mode growth rate, while the EM component grows with approximately twice the ITG growth rate, indicating a nonlinear excitation mechanism. Moreover, in the saturated nonlinear phase, bursts of EM flux appear with an approximately $2R/c_s$ delay from the ES components.

The electromagnetic transport mechanism described here is intrinsically nonlinear—i.e. it cannot be inferred in a straightforward way from the linear properties of the ITG modes. However, a simple empirical relationship has been identified between the electrostatic and electromagnetic components of the flux. The electromagnetic heat diffusivity is proportional to $\beta^2/\beta_{\mathrm{KBM}}^2$, where β_{KBM} denotes the KBM limit. The proportionality factor is of order unity in the cases examined (0.92 for the CBC case, and 0.24 for a TEM case). Thus, simple rules may be identified that allow quasilinear estimates to be extended to this nonlinear electromagnetic transport mechanism.

The above analysis shows that, in addition to magnetic stochasticity at very low β, ITG turbulence deviates from standard views of plasma turbulence in other ways. Zonal flows can no longer be viewed as purely beneficial. Through their role in mode coupling between the instability and stable microtearing fluctuations, they open an additional transport channel—the electron heat flux. Because this channel only arises through nonlinear energy transfer it cannot be obtained directly from quasilinear theory. It can only be related to quasilinear theory, as above, by making use of knowledge of the excitation spectrum of the stable tearing parity modes. Mode analysis that accounts for the finite amplitude of stable modes at the scales of the instability is critical for an understanding of saturation.

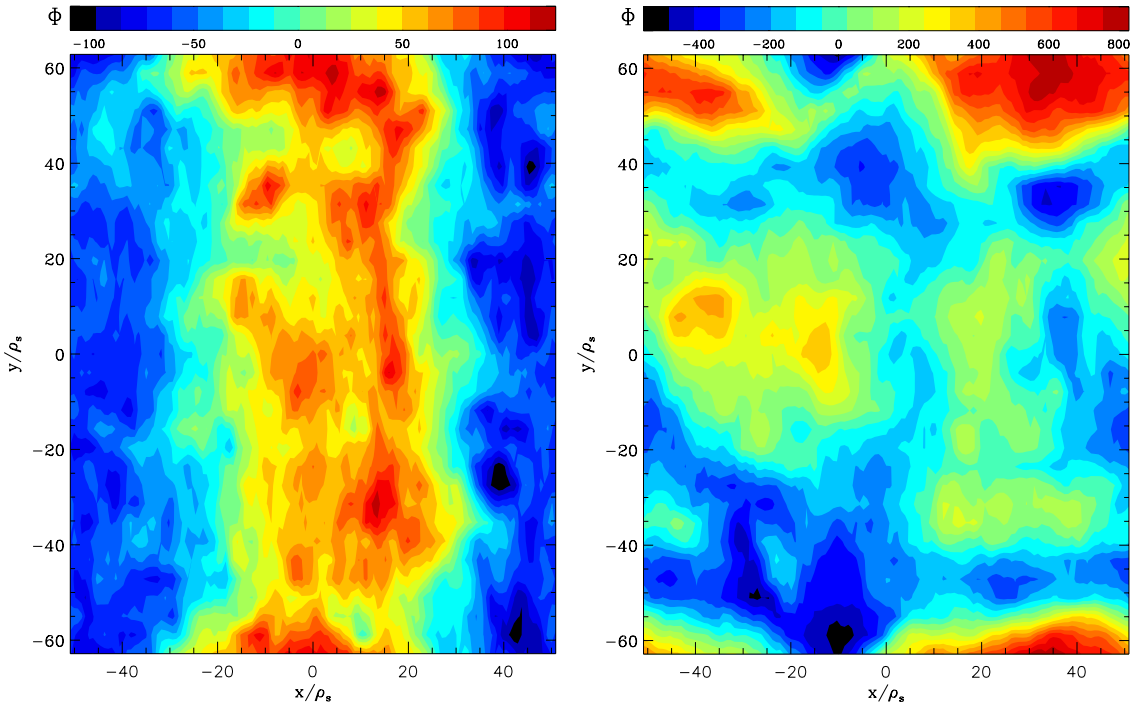

Figure 2. Potential contours in the nonlinear state of ITG turbulence. The left panel is for $\beta = 0.7\%$ (below the NZT threshold) and the right is for $\beta = 0.9\%$ (just above).

3. The non-zonal transition

In CBC, when β increases above 0.9% (~0.7 of the critical β for KBM instability) gyrokinetic codes fail to saturate at reasonable levels [30–32, 56, 57]. Because this runaway phenomenon is common to many codes, including gyrofluid codes [58] it is not a numerical artifact. One idea proposed as a physical basis for this phenomenon is that it represents a subcritical KBM instability (tertiary) of the secondary zonal flow structure driven by nonlinear profile corrugations of temperature and density [30]. A careful measurement of the corrugation amplitudes near the runaway threshold indicates that they are too small to destabilize KBMs subcritically at this β [31]. Furthermore, a consideration of electrostatic potential corrugations that self consistently accompany pressure corrugations, but were ignored in [30], shows that they can negate the effect of the pressure corrugations through their shear.

Here we describe a set of recent discoveries that point to the cause of the runaway phenomenon as arising instead from the depletion of zonal flows by radial motion of electrons streaming along strongly perturbed field lines. Zonal flows consequently lose their ability to saturate the linear instability, causing severely increased heat and particle flux levels. The phenomenon is labeled the non-zonal transition [31, 57]. Simulation of nonlinear dynamics above the NZT shows a saturated state with strongly reduced zonal flows. This is shown in the right panel of figure 2 and compared in the left panel with a case below the threshold.

That the reduction of zonal flows is caused by charge loss from rational surfaces associated with streaming along perturbed fields is demonstrated by two calculations. In one, the radial excursion of a perturbed field is increased until it exceeds the field-line correlation length, allowing for irreversible charge loss. The β associated with this condition matches the critical β for the NZT. In the second an external radial magnetic field perturbation is applied to a Rosenbluth–Hinton residual flow [59]. Prompt electron losses cause the potential response to swing through zero. The rate and its scalings are calculated from a closure theory for the mode coupling of the external field, and agree well with measurements from a numerical calculation of the potential response [60]. We focus below on the critical β for the NZT. The derivation of the threshold from field-line decorrelation allows us to infer key scalings. From variation with driving gradient we determine that the NZT does not occur at a set fraction of the KBM threshold. It can be higher than the KBM threshold or lower than the 0.9% value of $\beta_{\rm crit}$ for NZT in the CBC. From the dependencies on magnetic field scales we determine how this threshold changes in the RFP relative to the tokamak.

The critical β for transition occurs when a field line decorrelation criterion analogous to an island overlap condition is met [57]. An illustration of field line decorrelation is given in figure 3. Here, field line positions are obtained by integration (along the coordinate parallel to the guide field) of the perturbed magnetic field. Note that this picture requires no resonant perturbations, which have even parity in the magnetic potential; instead, purely quasilinear, odd-parity radial fluctuations B_x are sufficient to bring about this process. Starting from the inboard side (at the left of figure 3), field lines depart from their original radial position, marked by the unperturbed circular flux surface in black. For a correlated field line (red), the maximum radial displacement Δr is reached at the outboard side (on the right), and the second half turn brings the field line back to its original position, due to the

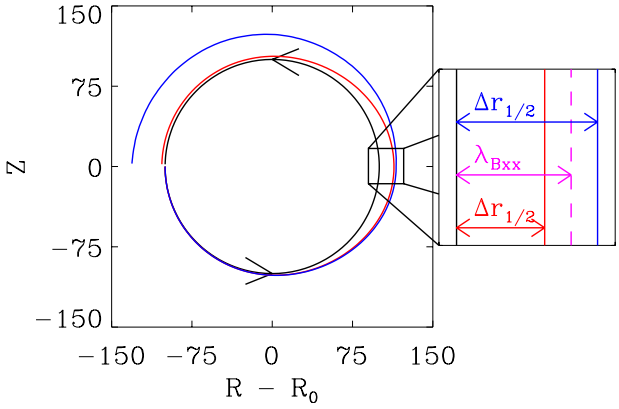

Figure 3. Illustration of field line decorrelation. Shown in the R–Z plane are the unperturbed flux surface in black, and two field lines subject to some nonresonant perturbation. The red field line remains correlated, whereas the blue one decorrelates and fails to return to its original radial position.

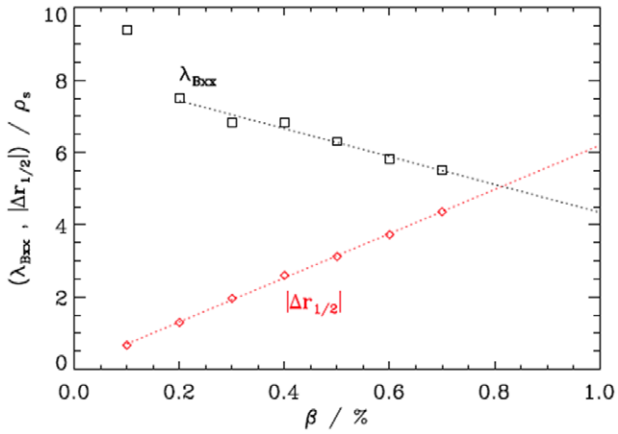

Figure 4. Variation with β of the half turn radial field line displacement $\Delta r_{1/2}$ and the radial correlation length λ_{Bxx} At the point where they cross an odd parity magnetic vector potential fluctuation is unable to return to the surface, defining the critical β for the NZT.

aforementioned odd parity. Given a sufficiently large B_x (e.g. due to a sizable β), it is possible for the outboard displacement $\Delta r_{1/2}$ to exceed the radial correlation length of B_x—which is the case for the blue field line, as illustrated in the magnified region on the right. Decorrelation, however, means that the onward trajectory of the field line is statistically independent of the previous path. While for the red line, the second half turn causes a displacement $\Delta r_{2/2} = -\Delta r_{1/2}$ that cancels the first half, returning charge to the surface, this is no longer the case for the blue line. Instead, the field line's displacement from the surface is irreversible, creating a radial charge path, radial currents, and irretrievable charge loss from flux surfaces. The process by which such radial currents are able to short out zonal flows is described in detail by the residual flow calculation of [60].

The displacement $\Delta r_{1/2}$ increases with the perturbation strength B_x. The radial correlation length λ_{Bxx} decreases moderately with β. The point where these two lengths become equal allows irretrievable charge loss and hence yields the observed critical β for NZT, as shown in figure 4. From figure 4 it is straightforward to predict what happens when the temperature gradient is increased. This gradient drives the turbulence; consequently an increase yields a larger value of B_x and $\Delta r_{1/2}$ for a given β. This increases the slope of $\Delta r_{1/2}$ in figure 4, thereby decreasing the critical β for NZT. Numerical measurements verify that a change in the crossing point of $\Delta r_{1/2}$ and λ_{Bxx} produces a like change in the critical β. In the CBC, the critical β for NZT is below the KBM threshold. However, for a weaker temperature gradient, the NZT threshold can occur at a higher β than the KBM threshold. For the General Atomics standard case [30] the gradients are steeper than CBC and the NZT threshold occurs below 50% of the KBM threshold.

Based on the above picture, it is possible to estimate the critical β for the NZT transition as a function of the temperature gradient. Relative to $\beta_{\rm crit}^{\rm KBM}$, the instability threshold for the KBM,

$$\frac{\beta_{\rm crit}^{\rm NZT}}{\beta_{\rm crit}^{\rm KBM}} \propto \frac{1}{(\omega_T - \omega_{T,\rm crit})^{\xi/2}}, \qquad (1)$$

where $\omega_T = -(\partial T/\partial r)R_0/T$, $\omega_{T,\rm crit}$ is the critical gradient for ITG instability, and $1/2 < \xi < 1$ [61]. From this expression it is clear that near the ITG temperature gradient threshold, the NZT critical β is above the KBM critical β. Conversely, for a sufficiently large temperature gradient, any system whose saturation is dependent on zonal flow activity may undergo an NZT. Since the non-zonal transition may, in principle, lead to very stiff limits, it is important to study its potential role in experimental scenarios. Ongoing research is focused on the transition between linear and saturated Ohmic confinement regimes, as well as on high-gradient regions such as the pedestal.

The analysis of the NZT in terms of a threshold for field line decorrelation and the quantitative agreement between numerical and analytical analyses of finite-β residual flow indicate a charge loss process from electrons streaming along perturbed field lines. This process is phenomenologically and conceptually distinct from the nonlinear processes that charge surfaces through turbulent Reynolds and Maxwell stresses. Therefore, one cannot be considered the negative of the other. The Maxwell stress has been hypothesized to partially cancel the Reynolds stress in driving zonal flows at finite β, thereby weakening zonal flows [39]. This is consistent with observations of a general weakening of zonal flow strength with increasing β [13, 28, 29] and works in a parallel sense with the NZT. However, the strength of the turbulent stresses varies smoothly with nonlinear amplitude, whereas the charge loss process associated with the NZT undergoes a critical transition. Moreover, in the residual flow calculation the charge loss associated with NZT is treated as a response to an impulsive force, whereas the Reynolds and Maxwell stresses are the force. A way of thinking about the distinctness of these two processes is provided by statistical closure theory, such as the direct interaction approximation, where there is a turbulent response that is quite distinct from the turbulent source, even though both derive from the same nonlinearity [62]. Of course, the turbulent stress and residual flow calculations have not been carried out jointly in a mutually consistent way, so there may be other connections. This question is presently under consideration in gyrokinetic analyses of electromagnetic nonlinear energy transfer at finite β [63].

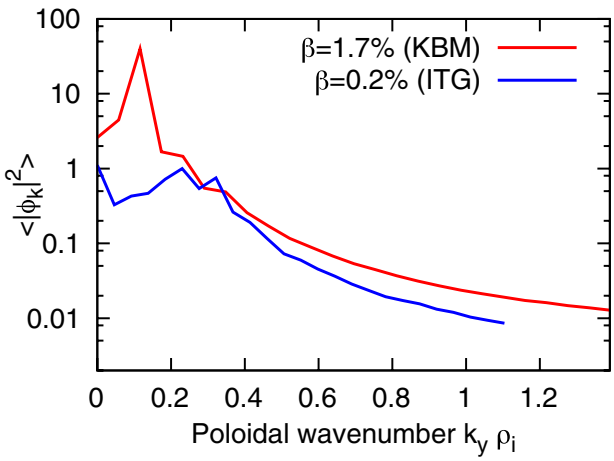

Figure 5. Spectrum of electrostatic potential $\langle|\phi_k|^2\rangle$ of the KBM turbulence in a helical plasma. Reproduced with permission from [64], Copyright 2014 AIP Publishing LLC.

4. Saturation of kinetic ballooning mode turbulence

In finite β toroidal plasmas, the growth of the ITG mode decreases with increasing β because of magnetic field line bending. Finite β ITG turbulence leads to a very high level of transport above a critical β (NZT). On the other hand, the KBM is destabilized at high β above another critical value, which is larger than the critical β of NZT for the CBC tokamak, and KBM turbulence does not become saturated in many computational scenarios.

However, there exist cases where high β turbulence with weak zonal flows is free from the saturation problem. When the electron temperature gradient is small, saturation of KBM turbulence is obtained with a physically relevant level of transport for tokamak and helical plasmas [47, 64–66], even when zonal flow production is weak. The weak zonal flow is shown by the electrostatic potential spectrum in a statistically steady state for a model of the standard configuration of the Large Helical Device in figure 5. The amplitude of the zonal component ($k_y = 0$) is comparable with the dominant mode for ITG turbulence at low β. On the other hand, the KBM turbulence has a sharp peak, and the zonal component ($k_y = 0$) is much smaller than the sharp peak of the KBM. Consequently, KBM turbulence saturation has two elements in common with saturation above NZT: β is high, implying magnetic effects, and zonal flows are weak.

In both the tokamak and helical plasma cases, the mode structure along the magnetic field line plays a central role in the saturation of the KBM turbulence. In the CBC-like tokamak plasma, the dominant KBM has an elongated mode structure along the magnetic field line because of fast streaming motion of electrons along the field line. The elongated structures acquire a twisting feature because of the magnetic shear, and the interaction between the KBM and the twisted structure leads to the saturation of the KBM. The twisted structure appears in the electrostatic potential profile in the (x, y)-plane with a high radial wavenumber in figure 6, while the KBM is represented by the horizontal stripes. The absence of noticeable vertical structure indicates that zonal flows are not a significant factor in saturation. In a helical plasma (the standard LHD plasma), the dominant KBM has a finite ballooning angle, i.e. it has a finite radial wavenumber, which is evident in the electrostatic potential profile in the right panel of figure 6. Since the three-dimensional magnetic field of the helical plasma has up-down symmetry, two oppositely inclined modes grow with the same growth rate. When their amplitudes become large, they interact with each other through nonlinear mode coupling, and the convection cells of the oppositely inclined modes shear each other, leading to saturation. Hence, the mutual shearing between the inclined modes, which have opposite ballooning angles, is the saturation mechanism of KBM turbulence in high β helical plasmas. The saturation process is qualitatively studied by evaluating the nonlinear entropy transfer function of interactions within triads of Fourier modes through nonlinear terms including electrostatic and magnetic perturbations.

For comparable growth rates, KBM turbulence is less efficient at transport than ITG turbulence, provided the turbulence undergoes a self interaction associated with elongated structure along the magnetic field [66, 67]. (The self interaction can be turned off, and the transport efficiency raised, by extending the simulation box along the field line.) When the self interaction limits transport, weaker zonal flows offset the effect: the ion heat flux for KBM is given by $Q_i^{\rm KBM} = 3n_0T_i\nu_{t_i}\rho_i^2/L_n^2$, while for ITG it is given by $Q_i^{\rm ITG} = 5n_0T_i\nu_{t_i}\rho_i^2/L_n^2$. The fluxes are comparable, with a slightly higher numerical coefficient for ITG.

5. Microtearing instability in tokamaks and RFPs

The microtearing mode (MTM), which is linearly stable for the CBC, has been predicted to be unstable for experimental core and edge conditions in the tokamak, the spherical tokamak, and the RFP. In conventional tokamaks MTM is typically weaker than ITG or TEM instabilities (e.g. [19]). However, for spherical tokamaks like NSTX and MAST, numerical solutions of gyrokinetic models using GYRO often predict the instability to be dominant in the core of high β H-mode plasmas [68], and to share some similarity to slab-theory predictions regarding β, electron temperature gradient, and collisionality [69]. Solutions of gyrokinetic models have identified two branches of the MTM instability, one which requires collisions and whose growth rate decreases with collisionality [71], and a collisionless branch [19, 21, 25, 48, 70]. For NSTX parameters the linear growth rate has a temperature-gradient threshold of $a/L_{T_e} \sim 1.3 - 1.5$. The transport fluxes grow sharply above $a/L_{T_e} = 2$, indicating a modest shift of the nonlinear threshold relative to the linear threshold. Because the mode is electromagnetic with a tearing parity mode structure there is also a critical threshold in β near a value of 4.5%. Finite collisionality is required for instability (with $Z_{\rm eff}\nu_{ei}/\omega$ not too large or small). Consequently MTM instability in NSTX is on the collisional branch. For this branch the time-dependent thermal force is important for instability, making the growth rate vanish in the limit of zero collisionality [71].

Fluxes from nonlinear simulations follow the same trends as the linear stability calculations, provided the saturated amplitudes ($\delta B/B$) are sufficiently large to ensure the onset of stochastic field lines. The electron heat flux, like that of the subdominant microtearing mode in CBC ITG turbulence, is well represented by magnetic flutter, with $\chi_e^{\rm EM} \sim$

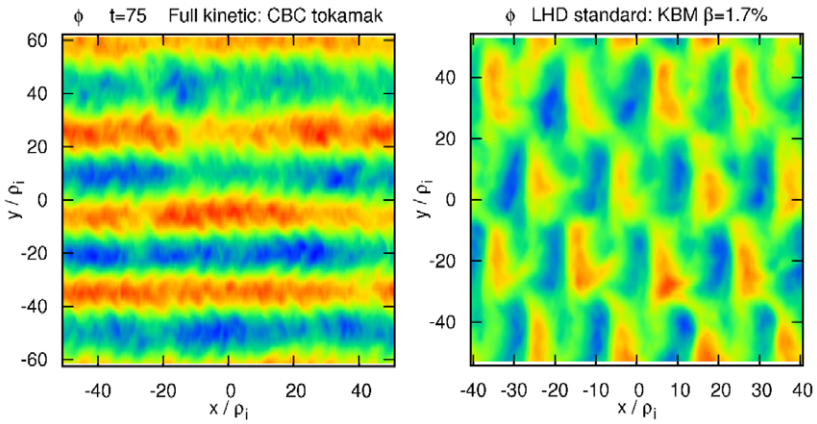

Figure 6. Color contours of electrostatic potential ϕ at the steady state of KBM turbulence in the CBC (left) and the standard LHD (right) with $\eta_e = 0$. Reproduced with permission from [47] (left), Copyright 2013 AIP Publishing LLC and [64] (right), Copyright 2014 AIP Publishing LLC.

$v_{\parallel,e}\delta B_r$. This follows the Rechester–Rosenbluth prediction [52] provided islands overlap, i.e. island widths exceed the spacing between rational surfaces. It is not clear what sets overall saturation and the scaling of δB_r in the gyrokinetic models, although there is a prediction from fluid theory that damped modes are excited to a sufficient level to provide a significant sink for saturation [72]. The dependence of instability on collisionality yields an electron heat flux that scales with the electron collision frequency ν_e to the first power. This is consistent with global confinement trends in NSTX that indicate an inverse scaling of confinement time with ν_*.

The MTM is also important in the RFX-mod RFP, where linear GS2 simulations performed for the experimental geometry show that MTMs are typically the fastest growing instabilities across the transport barriers occurring during the single helicity state [75]. For a selected set of RFX discharges the quasi-linear estimate of the electron conductivity, $\chi_e \sim (\rho_e/L_{T_e})v_{th,e}L_c$, turns out to be in good agreement with the experimental values [76], making MTM turbulence a major player for electron heat transport in the helical regimes. For the typical values of β in RFX-mod, MTM destabilization is obtained above $a/L_{T_e} \sim 2.5$–3 in the plasma core, an easily accessible value during the helical states. Work is in progress to extend the previous conclusions to a fully helical description, by means of the code GENE coupled to the helical VMEC equilibria of RFX.

Investigation of MTM stability covering a large parameter space has revealed that the collisionless branch of MTM is predicted to occur for certain experimental conditions often encountered in the RFP configuration, even neglecting the trapped electron dynamics. This branch does not require the time-dependent thermal force, and is therefore distinct from the branch of the MTM that appears in NSTX models. The decisive role of the curvature and grad-B drifts in destabilizing the mode is evident especially in the collisionless limit, as described in [25] and [48]. Retaining electrostatic potential fluctuations is always found to be destabilizing. An instability calculation for this new MTM branch has been undertaken, using a high frequency expansion for the propagator of the gyrokinetic equation in the collisionless regime. Temperature gradient free energy is accessed through the electron grad-B/curvature drift. Typically this drift has been neglected in analytic instability calculations of MTM growth, but in the RFP and spherical tokamak it is larger than its standard tokamak counterpart. In the RFP, the drift is larger by a factor of the aspect ratio. Instability requires a finite electrostatic potential. The mode represents the collisionless limit of a semicollisional tearing instability described previously [77]. However, besides the drifts, there is another destabilizing mechanism, which arises due to the mutual balance between magnetic shear, density gradient and electron temperature: a positive growth rate is accessible in the collisionless limit even without curvature and grad-B drifts in ω_d, provided the density profile is flat; again electrostatic potential fluctuations are destabilizing. Such results have been recovered with a more practical drift kinetic model [25], showing a qualitative agreement both on the role of the magnetic drifts and of density/safety factor profile. Collisionless MTM has also been found near the pedestal of spherical tokamaks [73, 74]. In particular, [73] also invokes magnetic drifts as a possible explanation, although with particle trapping.

An important aspect of microtearing instability in the RFP is its dependence on magnetic shear. The magnetic shear of the RFP is large and negative, and tends to increase with minor radius and the RFP pinch parameter $\Theta = \langle B_\theta \rangle^{\rm wall}/\langle B_\phi \rangle^{\rm vol}$. The growth rate decreases as the magnitude of the magnetic shear becomes larger. This is seen in figure 7, which shows linear GYRO runs for an RFP equilibrium model known as the toroidal Bessel function model [78]. The growth rate is shown as a function of collisionality for three values of the radius, with corresponding shear values $\hat{s}$ indicated. Here $\hat{s} = (r/q)(\mathrm{d}q/\mathrm{d}r)^{-1}$, where q is the safety factor. It is readily apparent that as the radius increases the magnetic shear becomes more negative and the growth rate decreases. It should be noted that while the expression for $\hat{s}$ is not accurate near the reversal surface where q vanishes, $\hat{s}$ is accurate to within 35% for the radial values of figure 7.

These plots also show the collisional and collisionless branches of the MTM, and suggest that the collisionless branch is more strongly stabilized by shear than the collisional branch. In figure 7 the two branches are most distinct at $r/a = 0.5$ ($\hat{s} = -0.7$), where different shapes are seen in the growth rate on either side of $\nu = 0.1$. This feature appears because only the

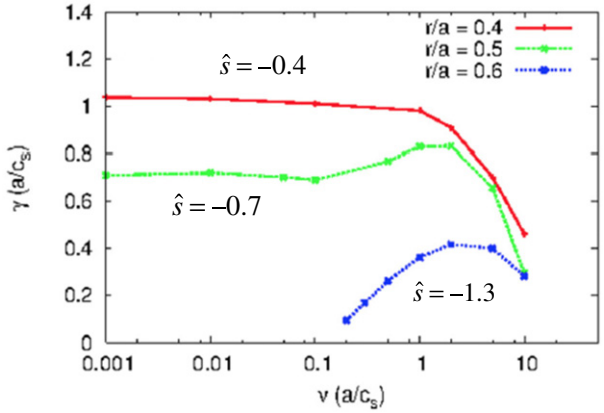

Figure 7. Growth rates for MTM as a function of collisionality for the toroidal Bessel function equilibrium. Three radial values are shown, with corresponding values of the magnetic shear. Adapted with permission from [14], Copyright 2013 AIP Publishing LLC.

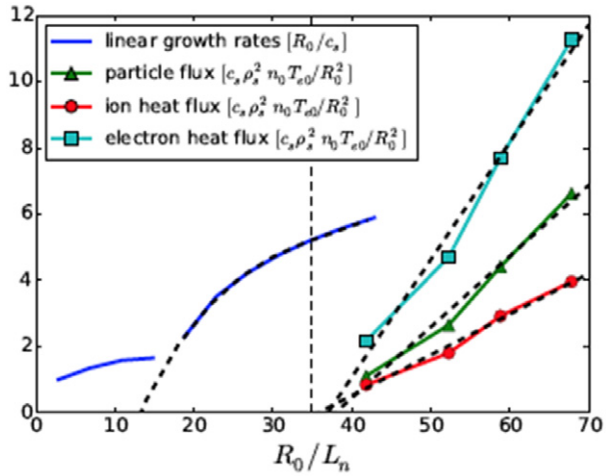

Figure 8. Growth rate, heat fluxes, and particle flux of TEM turbulence as a function of density gradient for an MST discharge of 500 kA. Straight-line fits have been applied to the fluxes, and a cubic fit to the TEM portion of the linear growth rate curve. The onset of the nonlinear fluxes occurs at $R_0/L_n \approx 37$, roughly a factor of 3 greater than the linear threshold of $R_0/L_n \approx 13$. Reproduced with permission from [48], Copyright 2015 AIP Publishing LLC.

growth rate of the fastest growing mode is plotted. Different branches are dominant on either side of the break. (A break, but not a discontinuity, also appears in the frequency at the same value of ν, as seen in figure 8 of [14].) The collisional branch corresponds to the peaked feature near $\nu = 2$. For $\nu < 0.2$ the collisionless branch takes over, and is relatively independent of ν down to the lowest colisionalities shown. The growth rates of both branches decrease as the shear becomes more negative, but the decrease is more marked on the collisionless branch. At $\hat{s} = -1.3$ the growth rate of the collisionless branch has become less than 0.1 and is not seen in figure 7, whereas at $\hat{s} = -0.4$, it becomes as large as the growth rate of the collisionless branch at its peak.

6. Microturbulence in MST

Prior analysis of microtearing instability has addressed specific discharges for RFX-mod, but not for the Madison Symmetric Torus (MST). While MST values for β and electron temperature gradient L_{T_e} can lie above thresholds, those thresholds have only been calculated for generic equilibria such as the toroidal Bessel function model [78]. We consider here specific MST experimental discharges with reduced tearing mode activity, achieved by flattening the current profile with pulsed poloidal current drive (PPCD). These discharges are selected because, unless tearing modes are reduced, their dominance of microturbulent fluctuations make the latter unobservable experimentally. Indeed, recent observations in PPCD plasmas using the laser interferometry diagnostic, show for the first time a distinct feature in the fluctuation spectrum that is independent of global tearing modes and the cascade to smaller scale that they drive [80]. PPCD discharges have a high value of Θ, for which the toroidal Bessel function model breaks down. To accommodate PPCD equilibria the circular equilibrium model of GENE has been modified with a form that accounts for the comparable values of the toroidal and poloidal field components and the radial variation of toroidal field [48]. The higher values of Θ in PPCD result in higher magnetic shear [78], with a pronounced effect on instabilities and turbulence.

Linear and nonlinear gyrokinetic simulations of two MST PPCD discharges, with 200 kA and 500 kA, draw equilibrium fields from MSTFit, electron temperature profiles from Thomson scattering and soft-x-ray tomography, and density profiles from far-infrared interferometry. Ion temperature profiles are not measured, so the GENE simulations assume that the ion temperature profile has the same shape as the electron profile with a peak value equal to 0.4 of the peak electron temperature. Despite β values ranging from 0.1% to 6.5%, unstable fluctuations, which are present in the edge ($r/a > 0.6$), are electrostatic in character: while producing a finite magnetic vector potential, its parity along the field line is odd. Moreover the growth rate of these fluctuations has little or no dependence on β over the range $0.1\% < \beta < 6\%$. Despite operating at a β that is considered high in the context of tokamaks, there is no MTM, KBM, or NZT. We comment specifically on the latter below, where we describe the presence of strong zonal flows in the nonlinear phase. The ratio of normalized density gradient to temperature gradient can vary strongly in PPCD discharges of different current, although not in a systematic way. The 200 kA discharge had a steeper temperature gradient than density gradient. On the basis of frequency, growth rate scalings with gradients, and mode structure, the fluctuations in the 200 kA discharge are identified as ITG at most radial locations. The 500 kA discharge has a steeper density gradient than temperature gradient, and its fluctuations are identified as TEM. Nonlinear simulations of the 500 kA discharge have a large level of zonal flows and a strong Dimits shift. Figure 8 shows an electron density gradient scan of the linear growth rate and nonlinear fluxes for electron heat, ion heat, and particles. The transport fluxes have a critical density gradient that is 3 times as large as the threshold for linear instability. This is considerably larger than the tokamak upshift of 1.5 at a similar β. The experimental density gradient is near the nonlinear critical gradient, suggesting that TEM may be setting the profile in the region where it is active.

The heat and particle fluxes of figure 8 are an order of magnitude lower than inferred fluxes in the 500 kA MST discharge. This discrepancy must be assessed in concert with other key features of the simulations—the large zonal flows observed in electrostatic potential contours, the large impact on transport as quantified by the Dimits shift, and the quiescent state of resonant magnetic fluctuations. In the context of section 3 this combination of features typifies plasmas well below the NZT. Why, then, are the experimental fluxes so high? The answer to that question is found in the fact that PPCD does not completely remove tearing mode activity. Magnetic fluctuations measurements in PPCD show that magnetic activity persists across the toroidal mode number spectrum, albeit at reduced level [79]. This residual level of resonant fluctuations and magnetic stochasticity arises from tearing modes and is not present in the GENE microturbulence simulations. Given the sensitivities documented in section 3 of fluxes on zonal flows, and zonal flows on magnetic fluctuations, a meaningful comparison of experimental and numerical fluxes requires that the stochasticity of the residual tearing modes be modeled in the simulations.

To address this issue an artificial Gaussian perturbation of $A_\parallel$ was introduced in the simulations. The perturbation had $k_x = 0$ and $k_y = 0.2$, making it resonant in B_x. The amplitude was tuned so that its resultant magnetic diffusivity matched experiment with a value of $D_m \sim 10^{-8}$. This is representative of the experimental diffusivity, although values are known only to within fairly large error bars. The magnetic perturbation introduced a small electromagnetic heat flux of order $3\,\mathrm{m^2\,s^{-1}}$. More importantly, it significantly reduced the zonal flows, and raised the electrostatic heat flux an order of magnitude to $25\,\mathrm{m^2\,s^{-1}}$. This exercise illustrates the importance of accurately modeling the residual stochasticity from tearing modes, while at the same time providing confirmation of the conclusions of section 3 about the effect of magnetic turbulence on zonal flows.

7. Effects of magnetic geometry

The conspicuous absence of microscale magnetic turbulence and a zonal-flow disabling NZT in gyrokinetic modeling of MST PPCD discharges leads us to examine the role of magnetic geometry on critical gradients and critical β values, and to contrast RFP and tokamak scalings. In toroidal geometry the poloidal and toroidal fields vary on the minor and major radius scales respectively. For tokamaks $B_\phi \gg B_\theta$, and for standard aspect ratio the scale lengths of the magnetic field variation and connection length are of order the major radius. In the RFP the poloidal and toroidal fields are the same order. Scale lengths and the connection length are of order the minor radius. The safety factor is smaller than ~0.2 and vanishes near the edge where the toroidal field reverses direction. These differences tend to affect stability and saturation in a way that uniformly pushes electromagnetic turbulence to much higher β for the RFP relative to the tokamak.

Consider first the gradient thresholds for both low and high β instabilities in the RFP. Gradient scans for ITG, MTM, and TEM show that the critical gradients for the RFP, measured in r/L_{crit}, fall in the same narrow range of 3–4 as those of the tokamak, with the latter measured in R/L_{crit}. Here r is the minor radius of the flux surface of interest. Consequently critical gradients for these instabilities are higher in the RFP than in the tokamak by a factor $\sim R/r$, i.e.

$$\frac{1}{L_{\mathrm{crit_{RFP}}}} = \left(\frac{R}{r}\right)\frac{1}{L_{\mathrm{crit_{Tok}}}}, \tag{2}$$

where L_{crit} is a density or temperature gradient scale length. This is consistent with differences of magnetic field scale lengths through thresholds for toroidal drift wave instabilities.

We consider next critical beta values for the thresholds of a variety of magnetic fluctuation effects. We recall that for the tokamak CBC the critical β for KBM instability and the ideal MHD β limit, usually called the high-n β limit, are very close ($\beta_{\mathrm{crit}}^{\mathrm{KBM}} \sim 0.9\beta_{\mathrm{MHD}}$) and track each other. For this reason both limits are used in the literature to mark the onset of electromagnetic modes. For CBC $\beta_{\mathrm{crit}}^{\mathrm{NZT}} = 0.7\beta_{\mathrm{crit}}^{\mathrm{KBM}}$, but as we have shown, changing gradients raises or lowers $\beta_{\mathrm{crit}}^{\mathrm{NZT}}$ relative to $\beta_{\mathrm{crit}}^{\mathrm{KBM}}$. In the RFP we anticipate that all critical β values will shift upward, in part because of magnetic shear. Familiar formulas for magnetic shear give the shear scale length as $L_S = qR/\hat{s}$, where the shear parameter $\hat{s}$ is given by $\hat{s} = (r/q)\mathrm{d}q/\mathrm{d}r$. These expressions are derived for tokamak geometry because they assume that $B_\phi \gg B_\theta$. Except very near the magnetic axis they are not appropriate for the RFP. In the outer part of the plasma where the gradients are strongest and instability growth rates are largest these expressions overestimate the strength of the shear. This is most evident at the reversal radius where $q = 0$, yielding $\hat{s} \to \infty$ and $L_S = 0$. In reality the shear remains well behaved and finite across the reversal radius and L_S does not become zero. Appropriate magnetic shear parameters for the outer part of an RFP plasma are derived by expanding $k_\parallel$ about a rational surface, just as is done to derive the tokamak parameters. For the RFP,

$$\mathrm{i}k_\parallel = \frac{i}{|B|}\left[\frac{B_\phi n}{R} - \frac{B_\theta m}{r}\right] = \frac{i}{B_\theta} r|B|\left[\frac{B_\phi r n}{RB_\theta} - m\right]. \tag{3}$$

We assume that B_θ, which is near a maximum, is slowly varying relative to B_ϕ, which is monotonically decreasing. We therefore treat B_θ as constant and expand $B_\phi(r)$ in a Taylor series about the rational surface that is resonant with m and n. The lowest order term $B_\phi(r_s)n/RB_\theta$ cancels with m on account of the resonance, and the next order term yields

$$\mathrm{i}k_\parallel \approx (r - r_s)\frac{\mathrm{i}n}{r}\frac{\mathrm{d}q}{\mathrm{d}r} = \mathrm{i}k_\phi\frac{(r - r_s)}{L_{S_{\mathrm{RFP}}}}, \tag{4}$$

where

$$L_{S_{\mathrm{RFP}}} = \frac{r}{\hat{s}_{\mathrm{RFP}}}, \tag{5}$$

and

$$\hat{s}_{\mathrm{RFP}} = R\frac{\mathrm{d}q}{\mathrm{d}r}. \tag{6}$$

We note that $\hat{s}_{\mathrm{RFP}}$ is finite and well behaved at the reversal surface and that $L_{S_{\mathrm{RFP}}}$ is nonzero. However, it remains true that magnetic shear in the RFP is stronger.

We quantify the change with the ratio of shear scale lengths, which from the above formulas is

$$\frac{L_{S_{\mathrm{Tok}}}}{L_{S_{\mathrm{RFP}}}} = q_{\mathrm{Tok}}\left(\frac{R}{r}\right)^2\frac{\mathrm{d}q_{\mathrm{RFP}}/\mathrm{d}r}{\mathrm{d}q_{\mathrm{Tok}}/\mathrm{d}r} \sim q_{0_{\mathrm{RFP}}}\left(\frac{R}{r}\right)^2, \tag{7}$$

where $q_{0_{\rm RFP}}$ is the safety factor on the axis. The large contribution of the square of the aspect ratio is partially offset by the safety factor, which is less than unity. However for typical values the shear scale length ratio has a magnitude comparable to the aspect ratio.

A critical β value governs the stabilization of ITG, which is adversely affected by magnetic fluctuations. This critical β is raised in the RFP geometry. A calculation of the stabilizing effect of self-consistent perpendicular magnetic field fluctuations at finite β leads to a critical β estimate given by

$$\beta \geqslant \epsilon_n \epsilon_t^2 \tau^2 [1 + (\epsilon_t/q_0)^2]^{-1} q_0^{-2} [(\tau + 2\epsilon_n)(\tau + 1) + \tau^2 \eta_e]^{-1}, \tag{8}$$

where ϵ_n is the ratio of the density to magnetic field scale length, $\epsilon_t = r_0/R_0$, $\tau = T_e/T_i$, and $\eta_e = {\rm d}\ln T_e/{\rm d}\ln n_0$. This expression has complicated dependencies, but yields a threshold for ITG stabilization that is higher in the RFP by a factor that is at least comparable to the aspect ratio. This is consistent with ITG stability analysis from gyrokinetics [14].

The critical β for NZT in the tokamak is 0.9% for the Cyclone base case. The RFP gyrokinetic modeling exercises described in the previous section showed no NZT up to a β of 6.5%. The critical β for NZT has been estimated for the tokamak and can be modified for the RFP as follows. In the edge where microinstability is active, the RFP connection length has a factor r/q_0R_0 relative to the tokamak connection length; ω_T has a factor r/R_0. Assuming that the radial magnetic correlation length does not change significantly from RFP to tokamak, the critical β for the NZT in the RFP relative to the tokamak goes as

$$\frac{\beta_{\rm crit}^{\rm NZT}|_{\rm RFP}}{\beta_{\rm crit}^{\rm NZT}|_{\rm Tok}} \propto \left(\frac{R_0}{r}\right)^{1+\xi/2} q_0|_{\rm Tok}. \tag{9}$$

Because the onset of many electromagnetic effects tracks the onset of KBM instability, we examine how it scales with RFP parameters. For tokamaks the critical β for KBM instability typically falls in the range 0.6% to 2%. We argue that the critical β increases markedly in the RFP due to high magnetic shear and low safety factor. We assume that the critical β for KBM occurs at a significant fraction of the critical β for ideal ballooning, as it does in the tokamak. We use the plasma ballooning parameter

$$\alpha_{\rm MHD} = \beta q^2 [R_0/L_n + R_0/L_{T_e} + (R_0/L_n + R_0/L_{T_i}) T_i/T_e], \tag{10}$$

and take the tokamak threshold for the critical MHD ballooning limit, $\alpha_{\rm MHD}^{\rm crit} = 0.6\hat{s}$, as a proxy, however using the expression $\hat{s}_{\rm RFP} = R{\rm d}q/{\rm d}r$ that is appropriate for the magnetic shear of the RFP in the outer part of the plasma. The critical β from this rough estimate is

$$\beta_{{\rm crit}_{\rm RFP}}^{\rm KBM} \sim 0.6 \frac{R/r}{q[R_0/L_n + R_0/L_{T_e} + (R_0/L_n + R_0/L_{T_i}) T_i/T_e]}, \tag{11}$$

which falls between 25% and 250%, depending on the parameter values of $\alpha_{\rm MHD}$.

We see that a variety of scalings affects the ratios of critical gradients and critical β values, but that generally the RFP values are larger than tokamak values by a factor that often is comparable to the aspect ratio. This increase, which allows steeper gradients, better confinement, and higher β in the RFP, applies to microinstability, and can be expected to affect microscale modes whether or not the plasma is subjected to PPCD. However, absent PPCD, global tearing modes, which are not subject to the above effects, dominate transport and set profiles, and the existence of favorable conditions for having reduced microturbulence is irrelevant. Only when global tearing mode activity can be suppressed, do the advantages of RFP geometry for microinstability become important.

8. Conclusions

Operating magnetic confinement devices at high β modifies the landscape of confinement-limiting instabilities, saturation mechanisms, and transport. New instabilities in the form of KBM and MTM arise, and key linear and nonlinear properties have been described, particularly for the spherical tokamak, the RFP, and helical devices. We show that KBM turbulence is able to saturate without significant zonal flows through the development of nonlinear structures with different forms in the tokamak and helical cases. At low β, ITG turbulence, which saturates by nonlinearly exciting damped modes, excites stable tearing parity modes. These break magnetic surfaces and produce magnetic fluctuation driven electron heat transport. Because the transport has no linear relationship with the instability driving the turbulence, its flux is intrinsically nonlinear. The presence of such magnetic fluctuations in ITG turbulence interferes with zonal flows above a critical β, leading to the non-zonal transition and a state with very large fluctuation levels. These finite β effects are generally adverse to good confinement. However, we also show that in configurations with high magnetic shear and low q like the RFP, the onset of these effects occurs only at higher critical gradients and higher β.

These studies show that saturation at finite β has nuanced behavior and complex feedback loops. As shown by the saturation structures of KBM and the nonlinear excitation of stable tearing parity modes in ITG turbulence, saturation must involve modification of the linear state, which can cause transport that is more a product of the saturation mechanism than the linear instability. The complexities of saturation lead to a situation where nonlinear structures understood to benefit confinement (specifically zonal flows), are only beneficial for one transport channel (ions), but simultaneously bad for another transport channel (electrons). Moreover, structures such as zonal flows can succumb to secondary effects they help create—in this case stable tearing parity modes that are catalyzed by zonal flows, but, at a critical β, enable charge loss from rational surfaces, thereby disabling the zonal flows. When this happens saturation must resort to more inefficient channels, raising fluctuation levels and transport rates.

Acknowledgments

This work was partially supported by US DOE Grant No. DE-FG02-89ER53291.

References

[1] Jenko F. and Dorland W. 2001 *Plasma Phys. Control. Fusion* **43** A141
[2] Falchetto G.L. Vaclavik J. Villard L. 2003 *Phys. Plasmas* **10** 1424
[3] Candy J. 2005 *Phys. Plasmas* **12** 072307
[4] Belli E.A. Candy and J. 2010 *Phys. Plasmas* **17** 112314
[5] Holod I. and Lin Z. 2013 *Phys. Plasmas* **20** 032309
[6] Chen Y. *et al* 2003 *Nucl. Fusion* **43** 1121
[7] Parker S.E. *et al* 2004 *Phys. Plasmas* **11** 2594
[8] Naulin V. *et al* 2005 *Phys. Plasmas* **12** 052515
[9] Scott B.D. 2005 *New J. Phys.* **7** 92
[10] Rewoldt G. Tang W.M. and Hastie R.J. 1987 *Phys. Fluids* **30** 807
[11] Zonca F. *et al* 1999 *Phys. Plasmas* **6** 1917
[12] Synder P.B. and Hammett G.W. 2001 *Phys. Plasmas* **8** 744
[13] Pueschel M.J. and Jenko F. 2010 *Phys. Plasmas* **17** 062307
[14] Carmody D. *et al* 2013 *Phys. Plasmas* **20** 052110
[15] Hazeltine R.D., Dobrott D. and Tang T.S. 1975 *Phys. Fluids* **18** 1778
[16] Drake J.F. and Lee Y.C. 1977 *Phys. Rev. Lett.* **39** 453
[17] Chen L., Rutherford P.H. and Tang W.M. 1977 *Phys. Rev. Lett.* **39** 460
[18] Callen J.D. 1977 *Phys. Rev. Lett.* **39** 1540
[19] Doerk H. *et al* 2011 *Phys. Rev. Lett.* **106** 155003
[20] Doerk H. *et al* 2012 *Phys. Plasmas* **19** 055907
[21] Applegate D.J. *et al* 2007 *Plasma Phys. Control. Fusion* **49** 1113
[22] Smith D.R. 2011 *Plasma Phys. Control. Fusion* **53** 035013
[23] Guttenfelder W. *et al* 2011 *Phys. Rev. Lett.* **106** 155004
[24] Guttenfelder W. *et al* 2012 *Phys. Plasmas* **19** 056119
[25] Predebon I. and Sattin F. 2013 *Phys. Plasmas* **20** 040701
[26] Smolyakov A.I. 1989 *Sov. J. Plasma Phys.* **15** 667
[27] Connor J.W. *et al* 1990 *Plasma Phys. Control. Fusion* **49** 1113
[28] Pueschel M.J. *et al* 2008 *Phys. Plasmas* **15** 102310
[29] Citrin J. *et al* 2013 *Phys. Rev. Lett.* **111** 155001
[30] Waltz R.E. 2010 *Phys. Plasmas* **17** 072501
[31] Pueschel M.J. *et al* 2013 *Phys. Rev. Lett.* **110** 155005
[32] Pueschel M.J. *et al* 2013 *Phys. Plasmas* **20** 102308
[33] Nevins W.M. *et al* 2011 *Phys. Rev. Lett.* **106** 065003
[34] Hatch D.R. *et al* 2012 *Phys. Rev. Lett.* **108** 235002
[35] Hatch D.R. *et al* 2013 *Phys. Plasmas* **20** 012307
[36] Terry P.W., Baver D.A. and Gupta S. 2006 *Phys. Plasmas* **13** 022307
[37] Hatch D.R. *et al* 2011 *Phys. Rev. Lett.* **106** 115003
[38] Tatsuno T. *et al* 2009 *Phys. Rev. Lett.* **103** 015003
[39] Diamond P.H. *et al* 2005 *Plasma Phys. Control. Fusion* **47** R35
[40] Dorland W. *et al* 2000 *Phys. Rev. Lett.* **85** 5579
[41] Daughton W., Roytershteyn V. and karimabadi H. 2011 *Nat. Phys.* **7** 539
[42] Pueschel M.J. *et al* 2014 *Astrophys. J. Suppl.* **213** 30
[43] Hatch D.R. *et al* 2013 *Phys. Rev. Lett.* **111** 175001
[44] Hatch D.R. *et al* 2014 *J. Plasma Physics* **80** 531
[45] Makwana K. *et al* 2014 *Phys. Rev. Lett.* **112** 095002
[46] Kim J.-H. and Terry P.W. 2010 *Phys. Plasmas* **17** 112306
[47] Ishizawa A. *et al* 2013 *Nucl. Fusion* **53** 053007
[48] Carmody D. *et al* 2015 *Phys. Plasmas* **22** 012504
[49] Moradi S. *et al* 2012 *Phys. Plasmas* **19** 032301
[50] Albergante M. *et al* 2011 *Plasma Phys. Control. Fusion* **53** 054002
[51] Citrin J. *et al* 2015 *Plasma Phys. Control. Fusion* **57** 014032
[52] Rechester A.B. and Rosenbluth M.N. 1978 *Phys. Rev. Lett.* **40** 38
[53] Wang E. *et al* 2011 *Phys. Plasmas* **18** 056111
[54] Hatch D.R. *et al* 2011 *Phys. Plasmas* **18** 055706
[55] Terry P.W. *et al* 2014 *Phys. Plasmas* **21** 122303
[56] Nevins W.M. *et al* 2009 *Bull. Am. Phys. Soc.* **54** 35
[57] Pueschel M.J. *et al* 2013 *Phys. Plasmas* **20** 102301
[58] Scott B.D. 2006 *Plasma Phys. Control. Fusion* **48** B277
[59] Rosenbluth M.N. and Hinton F. 1998 *Phys. Rev. Lett.* **80** 724
[60] Terry P.W. *et al* 2013 *Phys. Plasmas* **20** 112502
[61] Pueschel M.J. *et al* 2014 *Phys. Plasmas* **21** 055901
[62] Orszag S.A. 1973 Statistical theory of turbulence *Fluid Dynamics* ed R. Balin and J.L. Peube (London: Gordon and Breach) p 237
[63] Whelan G.G. *et al* 2014 *Bull. Am. Phys. Soc.* **59** 318
[64] Ishizawa A. *et al* 2014 *Phys. Plasmas* **21** 055905
[65] Maeyama S. *et al* 2014 *Phys. Plasmas* **21** 052301
[66] Ishizawa A. *et al* 2015 *J. Plasma Phys.* **81** 435810203
[67] Beer M.A., Cowley S.C. and Hammett G.W. 1995 *Phys. Plasmas* **2** 2687
[68] Guttenfelder W. *et al* 2013 *Nucl. Fusion* **53** 093022
[69] Gladd N.T. *et al* 1980 *Phys. Fluids* **23** 1182
[70] Swamy A.K. *et al* 2014 *Phys. Plasmas* **21** 082513
[71] Hassam A. 1980 *Phys. Fluids* **23** 2493
[72] Makwana K. *et al* 2011 *Phys. Plasmas* **18** 012302
[73] Dickinson D. *et al* 2012 *Phys. Rev. Lett.* **108** 135002
[74] Canik J.M. *et al* 2013 *Nucl. Fusion* **53** 113016
[75] Predebon I. *et al* 2010 *Phys. Rev. Lett.* **105** 195001
[76] Carraro L. *et al* 2013 *Nucl. Fusion* **53** 073048
[77] Finn J.M. and Drake J.F. 1986 *Phys. Fluids* **11** 3672
[78] Tangri V. *et al* 2011 *Phys. Plasmas* **18** 052310
[79] Sarff J.S. *et al* 2003 *Plasma Phys. Control. Fusion* **45** A457
[80] Duff J. *et al* 2014 *Bull. Am. Phys. Soc.* **59** 253